Continuity of Microscopic Cardiac Conduction in a Computational Cell-by-Cell Model

Joshua Steyer[1], Fatemeh Chegini,[2] Mark Potse[3], Axel Loewe[1], Martin Weiser[2]

[1] Karlsruhe Institute of Technology (KIT), Institute of Biomedical Engineering, Karlsruhe, Germany
[2] Zuse Institute Berlin, Berlin, Germany
[3] LIRYC, Pessac, France

Abstract

Conduction velocity in cardiac tissue is a crucial electrophysiological parameter for arrhythmia vulnerability. Specifically, pathologically reduced conduction velocity facilitates arrhythmogenesis because such conduction velocities decrease the wavelength with which re-entry may occur. Computational studies on CV and how it changes regionally in models at spatial scales multiple times larger than actual cardiac cells exist. However, microscopic conduction within cells and between them have been studied less. In this work, we study the relation of microscopic conduction patterns and clinically observable macroscopic conduction using an extracellular-membrane-intracellular model which represents cardiac tissue with these subdomains at subcellular resolution. By considering cell arrangement and non-uniform gap junction distribution, it yields anisotropic excitation propagation. This novel kind of model can for example be used to understand how discontinuous conduction on the microscopic level affects fractionation of electrograms in healthy and fibrotic tissue. Along the membrane of a cell, we observed a continuously propagating activation wavefront. When transitioning from one cell to the neighbouring one, jumps in local activation times occurred, which led to lower global conduction velocity than locally within each cell.

1. Introduction

Being one of the main reasons for sudden cardiac death, which causes around 700,000 deaths per year in Europe alone, cardiac arrhythmias remains a major public health issues [1]. An important tissue property affecting arrhythmia vulnerability is the conduction velocity (CV) of cardiac excitation waves, which can be derived from local activation times (LATs), defined as the moment at which the excitation wave front reaches a certain point in space. The spatial distribution [2] and effect [3] of these quantities have been investigated in homogenised models. Such models, however, do not directly consider myocyte size and shape, an inhomogeneous arrangement of them, connectivity patterns, and microscopic conduction from cell to cell.

In this study, we investigate the distribution of LAT and CV values using the recently proposed extracellular-membrane-intracellular (EMI) model, which explicitly represents the extra- and intracellular space, as well as the membrane in the mesh [4, 5]. To do so, we used a 3D myocyte configuration embedded in a bath for which excitation propagation is initiated for three different cases to study purely longitudinal and transversal wave propagation, as well as a combination of them. We then determined LATs both on the membrane and the intracellular space and derived local CV, which were both analysed in terms of difference between the local (subcellular and cell-to-cell) and global behaviour of the excitation propagation.

2. Methods

We used the EMI model described in [4], which represents the extracellular medium Ω_e, the cell-to-cell membranes Γ_g, the cell-to-extracellular membrane Γ_m and the intracellular domain Ω_i explicitly in the mesh. Its model equations read

$$\begin{cases} \nabla\cdot(\sigma_\mathrm{i}\nabla\phi_\mathrm{i}) = 0 & \text{in } \Omega_\mathrm{i}, \\ \nabla\cdot(\sigma_\mathrm{e}\nabla\phi_\mathrm{e}) = 0 & \text{in } \Omega_\mathrm{e}, \\ V_\mathrm{m} = \phi_\mathrm{i} - \phi_\mathrm{e} & \text{on } \Gamma_\mathrm{m}, \\ w_\mathrm{g} = \phi_j - \phi_k \text{ where } j \neq k & \text{on } \Gamma_\mathrm{g}, \\ C_\mathrm{m}\dot{V}_\mathrm{m} + I_\mathrm{ion} = -n_\mathrm{i}^\mathrm{T}\sigma_\mathrm{i}\nabla\phi_\mathrm{i} = n_\mathrm{e}\sigma_\mathrm{e}\nabla\phi_\mathrm{e} & \text{on } \Gamma_\mathrm{m}, \\ C_\mathrm{m}\dot{w}_\mathrm{g} + I_\mathrm{g} = -n_j^\mathrm{T}\sigma_\mathrm{i}\nabla\phi_j = n_k\sigma_\mathrm{i}\nabla\phi_k & \text{on } \Gamma_\mathrm{g}, \end{cases} \tag{1}$$

where ϕ denotes the potential of the corresponding domain, while V_m describes the membrane voltage between Ω_i and Ω_e, and w_g between two different cell domains, Ω_j and Ω_k. n denotes the outer normal of the respective domain and the conductivities of the intra- and extracellular domains are $\sigma_\mathrm{i} = 0.3\,\mathrm{S/m}$ and $\sigma_\mathrm{e} = 2.0\,\mathrm{S/m}$,

and the membrane capacitance is $C_\mathrm{m} = 10^{-4}\,\mathrm{F/m^2}$. To model membrane dynamics, we used the Aliev-Panfilov model [6] with its ion current given by

$$I_\mathrm{ion}(V_\mathrm{m}, v) = g_a V_\mathrm{m}(V_\mathrm{m} - a)(V_\mathrm{m} - 1) + V_\mathrm{m} v, \quad (2)$$

and the gating dynamics being governed by

$$\frac{\partial v}{\partial t} = -\frac{1}{4}\varepsilon(V_\mathrm{m}, v)(v + g_s V_\mathrm{m}(V_\mathrm{m} - a - 1)), \quad (3)$$

where $\varepsilon(V_\mathrm{m}, v) = \varepsilon_0 + \mu_1 v/(V_\mathrm{m} + \mu_2)$, $g_a = g_s = 8.0$, $a = 0.1$, $\varepsilon_0 = 0.01$, $\mu_1 = 0.07$ and $\mu_2 = 0.3$. Being purely phenomenological, the normalised state variables of the dynamics V_m and v are restricted to [0,1] a.u. Similar to [7], we used a linear (Ohmic) relationship between the current through the gap junctions and the respective voltage between the two cells:

$$I_\mathrm{g} = \frac{w_\mathrm{g}}{R_\mathrm{g}}, \quad (4)$$

where $R_\mathrm{g} = 4.5 \cdot 10^{-4}\,\Omega\mathrm{m}^2$. This system was solved using the Kaskade 7 finite element toolbox [8].

The 3D mesh, generated by the Mmg remeshing software [9], is shown in Fig. 1. Its dimensions are 400 µm× 240 µm× 240 µm and it consists of approximately $5 \cdot 10^5$ tetrahedral mesh elements. The intracellular domain, Ω_i comprises $n_x \times n_y \times n_z = 7 \times 3 \times 7 = 147$ myocytes. The myocytes' largest extension (i.e., preferential orientation) is along the x-axis, which is thus the direction of fastest propagation and may be referred to as longitudinal direction. For transversal direction, we consider the y-axis. The intercalated discs with the gap junctions are located at $x = 150, 250$µm along the longitudinal axis, such that we have two planes (y, z) with gap junction properties given by Eq. 4. In total, we ran three different simulations with different initial conditions leading to different excitation dynamics: a) initial depolarisation of all leftmost myocytes along the x-axis (causing an almost purely longitudinal propagation and referred to as the **left** case), b) depolarisation of all lowermost cells (purely transversal propagation, **bottom** case) and c) depolarisation of one cell in the corner of the myocyte configuration (longitudinal and transversal propagation, **single** case).

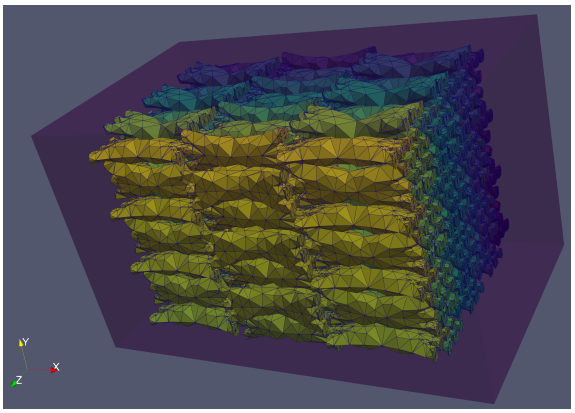

Figure 1: Myocyte arrangement used for the simulations embedded in Ω_e (semi-transparent purple box). Different colours correspond to different cells.

To quantify the spatial propagation of the excitation along the cell membrane (quantified via $V_\mathrm{m}(\boldsymbol{x}, t)$) and the intracellular potential ($\phi_\mathrm{i}(\boldsymbol{x}, t)$), where $\boldsymbol{x} \in \mathbb{R}^3$ denotes the position, we chose $V_\mathrm{m}^\mathrm{th} = 0.5\,\mathrm{a.u}$ and $\phi_\mathrm{i}^\mathrm{th} = 0.45\,\mathrm{a.u.}$ as thresholds to determine the local activation times (LATs). Using a projection of these LAT values onto the primary axis of propagation, i.e. either x or y, we then defined longitudinal and transversal CVs as:

$$\mathrm{CV_l}(\boldsymbol{x}) = \left|\frac{\partial \mathrm{LAT}(\boldsymbol{x})}{\partial x}\right|^{-1}, \quad (5)$$

$$\mathrm{CV_t}(\boldsymbol{x}) = \left|\frac{\partial \mathrm{LAT}(\boldsymbol{x})}{\partial y}\right|^{-1}. \quad (6)$$

3. Results

We first analyse LATs obtained from $V_\mathrm{m}(\boldsymbol{x}, t)$, along the propagation directions. The projections of LAT values along these axes are given in Fig. 2. For all cases, we fitted a linear function to a) the data within each "column" of cells (perpendicular to the propagation direction, green lines) and b) the complete data set (red line). The upper left panel shows the projection of LAT values of the central and right myocyte columns onto the x-axis (i.e. the axis of propagation). Both values grow linearly in propagation direction distance with a jump at the intercalated disc ($x = 250$µm). The upper right panel illustrates the distribution of LAT values along the transversal axis obtained from the "bottom" case. Note that, in contrast to the fully longitudinal propagation, the separate myocyte planes overlap, since the cells are intertwined both along the y and z direction (Fig. 1). Finally, for the depolarisation of one cell in the corner, we can project the LATs onto both the longitudinal and transversal direction, given in the bottom row of Fig. 2, respectively. While the LATs in transversal direction show linear growth in propagation direction, both within the myocyte planes and globally, the longitudinal data for this initialisation does not show a clear trend and is broadly distributed.

We now quantify the time delay of the activation propagation when transitioning from one myocyte to the next via the gap junctions in the intercalated disc. Both the mean and standard deviation of the LAT delays ΔLAT are given in Tab. 1.

The local and global CVs defined as the inverse slopes

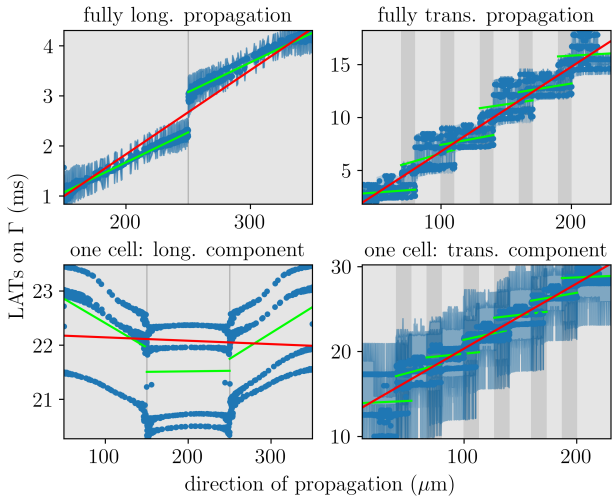

Figure 2: Spatial distribution of LAT values on the membranes as projections onto the axis of propagation. Green lines indicate the linear regression of LAT values within one column of myocytes and the red line the linear regression of all LATs along this axis. Dark grey background indicates intercalated disc regions, which are wider in the right column due to intertwining of myocytes along the y-axis. Bottom row: diagonal excitation starting from a single myocyte in the bottom left corner of the mesh.

propagation	ΔLAT (ms)
fully long.	0.8
fully trans.	1.7 ± 0.9
long. (single)	-0.2 ± 0.5
trans. (single)	1.6 ± 0.7

Table 1: Mean and standard deviation of LAT delays on the membrane during transition from one cell layer to the neighbouring one.

of the single myocyte column regressions and the inverse of the global slope, according to Eq. 6, are given in Tab. 2. Overall, the global CVs are smaller than the locally determined ones.

4. Discussion

We have analysed local CV values in the EMI model [4, 5], which explicitly represents intra- and extracellular media, as well as the membrane separately in the mesh. As opposed to what would be possible with homogenised models as the frequently used monodomain or bidomain models [10], this allowed studying the the local behaviour of the potential propagation. We have shown that LATs undergo jumps when the wave transitions from one myocyte to the next. CVs, calculated by the inverse slope of the linearly fitted LAT values reveal that the potential and excitation propagation within a cell is faster than globally, which in turn can be explained by the time delay in the order of few milliseconds caused at each cell-to-cell transition. The absolute value of global and local CV is a result of the choice of model parameters and gap junction distribution [11]. The setup used here motivated by previous work led to CV values one to two orders of magnitude smaller than typically observed in healthy human tissue [2, 12].

propagation	loc. $\overline{\text{CV}}$ (m/s)	glob. CV (m/s)
fully long.	0.0839 ± 0.0005	0.06
fully trans.	0.07 ± 0.04	0.01
long. (single)	1.2 ± 3.0	0.1
trans. (single)	0.08 ± 0.07	0.01

Table 2: Mean and standard deviation of the single myocyte layer LAT slopes and the global one along propagation direction x_i.

There are several limitations to this analysis. First, the analysis of transversal and diagonal CV should be refined by accounting for myocyte intertwining through local analysis coordinate systems with respect to each myocyte. Furthermore, we assumed the intracellular medium to be homogeneous without considering potential conduction anisotropy due to e.g. the nucleus or other organelles in the cell.

The findings presented here provide a first insight into electrophysiological excitation propagation behaviour (CV) on a microscale. It forms a basis for future work analyzing for example the genesis of intracardiac electrograms in such microstructural models [13] or extending the setup to pathological scenarios allowing for mechanistical studies of the role of microscopic cell arrangement and distribution of e.g. fibrosis.

Acknowledgments

This project has received funding from the European High-Performance Computing Joint Undertaking EuroHPC (JU) under grant agreement No 955495. The JU receives support from the European Union's Horizon 2020 research and innovation programme and France, Italy, Germany, Austria, Norway, Switzerland.

References

[1] Chugh SS. Sudden cardiac death in 2017: Spotlight on prediction and prevention. International Journal of Cardiology. (2017);237:2-5.

[2] Verma B, Oesterlein T, Loewe A, Luik A, Schmitt C, Dössel O. Regional conduction velocity calculation from clinical multichannel electrograms in human atria. vol. 92. Elsevier; 2018. p. 188-96.

[3] Azzolin L, Eichenlaub M, Nagel C, Nairn D, Sanchez J, Unger L, et al. Personalized ablation vs. conventional ablation strategies to terminate atrial fibrillation and prevent recurrence. Europace. 2023 2;25(1):211-22.

[4] Tveito A, Mardal KA, Rognes ME. Modeling Excitable Tissue: The EMI Framework. Simula Springer Briefs on Computing. Springer International Publishing; 2020.

[5] Jæger KH, Edwards AG, Giles WR, Tveito A. From Millimeters to Micrometers; Re-introducing Myocytes in Models of Cardiac Electrophysiology. Frontiers in Physiology. 2021;12:763584.

[6] Aliev RR, Panfilov AV. A simple two-variable model of cardiac excitation. Chaos, Solitons & Fractals. 1996;7(3):293-301.

[7] Chegini F, Steinke T, Weiser M. Efficient adaptivity for simulating cardiac electrophysiology with spectral deferred correction methods. In: Submitted; 2022. .

[8] Weiser M, Chegini F. Higher-order time integration using spectral deferred correction method (SDC) in a cell by cell discretization of cardiac excitation. Martin Weiser, Fatemeh Chegini; 2022. Available from: https://doi.org/10.35097/716.

[9] Dapogny C, Dobrzynski C, Frey P. Three-dimensional adaptive domain remeshing, implicit domain meshing, and applications to free and moving boundary problems. J Comp Phys. 2014;262:358-78.

[10] Plank G, Loewe A, Neic A, Augustin C, Huang YL, Gsell MAF, et al. The openCARP simulation environment for cardiac electrophysiology. Comput Methods Programs Biomed. 2021 6;208:106223.

[11] Rosilho de Souza G, Pezzuto S, Krause R. Effect of Gap Junction Distribution, Size, and Shape on the Conduction Velocity in a Cell-by-Cell Model for Electrophysiology. In: Bernard O, Clarysse P, Duchateau N, Ohayon J, Viallon M, editors. Functional Imaging and Modeling of the Heart. vol. 13958 of Lecture Notes in Computer Science. Cham: Springer; 2023. p. 117-26.

[12] Lubrecht JM, Grandits T, Gharaviri A, Schotten U, Pock T, Plank G, et al. Automatic reconstruction of the left atrium activation from sparse intracardiac contact recordings by inverse estimate of fibre structure and anisotropic conduction in a patient-specific model. EP Europace. 2021 Mar;23(Supplement_1):i63-70.

[13] Steyer J, Diaz LPM, Unger LA, Loewe A. Simulated Excitation Patterns in the Atria and Their Corresponding Electrograms. In: Bernard O, Clarysse P, Duchateau N, Ohayon J, Viallon M, editors. Functional Imaging and Modeling of the Heart. Cham: Springer Nature Switzerland; 2023. p. 204-12.

Address for correspondence:

Joshua Steyer
Institute of Biomedical Engineering
Karlsruhe Institute of Technology (KIT)
Fritz-Haber-Weg 1, 76131 Karlsruhe, Germany
publications@ibt.kit.edu